Plasmon Response and Structure of Nanocrystalline Diamond Powder

by

L.A. BURSILL, J.L. PENG and S. PRAWER

School of Physics, The University of Melbourne
Parkville, 3052, Vic., Australia

Abstract

High-resolution transmission electron microscopy, electron diffraction and parallel electron energy loss spectroscopy are used to analyse nanocrystalline diamond powder. Grains of diameter in the range 2- 10 nm were found aggregated together; the grain boundaries were essentially a grossly disordered (amorphous) intergranular phase. Analysis of the plasmon loss-function indicated mass density of 3.30 g/cm^3, compared with 3.51 g/cm^3 for a chemically-vapour-deposited diamond. The core-loss spectra showed virtually pure sp^3 bonding overall although some exposed surfaces were coated with two or three graphitic layers. Two peaks were observed in the low energy loss-function, one at 34 eV was characteristic of the volume plasmon typically observed in crystalline diamond, a second peak at approx. 23 eV for larger grains shifted to lower energies as the particle size decreased (to 19.5 eV for 2.8 nm diameter) and at the same time it increased in intensity, becoming stronger than the volume plasmon for a 2.8 nm crystal. These results are interpreted using theoretical results for surface plasmons in small spherical particles.

1. Introduction

In this paper, a combination of high-resolution transmission electron microscopy (HRTEM), electron diffraction (ED) patterns and parallel electron energy loss spectroscopy (PEELS) microanalysis techniques were used to analyse a nanocrystalline diamond powder (NDP). Studies by Erskine and Nellis (1992) showed that for graphite with sufficient orientational order a martensitic transition to a diamond-like phase is observed with a transition onset pressure 19.6 $\pm$ 0.7 GPa; more generally, diamond-like-carbons (DLC) result provided sufficient overpressures are applied, regardless of the nature of the original graphites. HRTEM studies of diamond powders were made in order to determine the degree of preferred orientation, grain size and phase purity. PEELS analysis showed our NDP to be essentially pure sp^3 bonded, as reported below. We also observed plasmon energies which showed shifts with particle size which are explained using theoretical results for small spherical particle models. We show that the changeover from characteristic "bulk" to "nanoscale" dielectric response occurs for particle size below $\approx$ 10 nm for diamond. This NDP also gave some interesting new sharp lines when examined by micro-Raman spectroscopy (Prawer, Nugent et al 1996). HRTEM and PEELS analysis results for chemical vapour deposited diamond (CVD) are also included for comparative purposes.

2. Experimental

Small portions of NDP were dispersed in distilled water, then centrifuged at 15000 rpm for 10 min. The aim of centrifuging the specimens was to separate different powder components and possible impurity phases having different densities. Two samples were examined by HRTEM/ED/PEELS; the source powder and a high density grey powder fraction obtained after centrifuging. These powders were first dispersed in water and then a small drop was placed onto clean, dry copper specimen support grids and examined in an electron microscope.

Images were recorded using a JEOL-4000EX electron microscope operating at 400 kev. A Gatan Parallel Detection Electron spectrometer (Model 666) attached to a JEOL-4000EX electron microscope was used to obtain the energy loss data at 100 keV; the resolution of the spectra was determined by measuring the full width at half-maximum (FWHM) of the zero-loss peak; this was typically close to 1.4 eV. In this case the beam diameter was typically 400 nm, the collection angle was 20 mrad, the beam convergence was 1 mrad and the spectra were recorded at 0.05 eV/channel. Additional PEELS data were obtained using a Phillips CM20 instrument operating at 200 keV. The energy resolution was again 1.4 eV but this instrument had the advantage that we could focus a 2 nm electron probe onto individual nanocrystals; a disadvantage was that the image resolution was insufficient to reveal lattice fringes, although it was

adequate to determine the diamenter of the particle under examination. These spectra were collected at 0.05 eV/channel with convergence angle 5 mrad and collection angle 15 mrad. For comparison purposes, the HRTEM images and the PEELS spectra of both NDP and CVD were acquired under identical experimental conditions.

3. PEELS Analysis Procedures

All spectra were deconvoluted to obtain the single scattering distribution (SSD) using the Fourier-Log method (Egerton, 1986) and the zero-loss peaks removed. Both of these processes were carried out using the Gatan EL/P software (version 2.1.1). The deconvolution was not always successful; this was primarily due to thickness variations of the specimen within the electron probe and use of the 1-2 nm probe of the CM20 noticeably improved this situation. Spectra which did not behave on deconvolution were rejected for subsequent analysis. The loss-function was then obtained, agin using standard EL/P software. The density was determined from the low-loss plasmon peak position using standard methods (Egerton, 1986; Peng et al, 1996).

4. Results and Analysis

(a) HRTEM and ED

Fig.1 shows a typical HRTEM image from CVD diamond, note the [110] zone lattice fringes parallel to (111) and ($\bar{1}11$); there are some stacking faults visible on these planes. Note also the surface layer some 1 nm thick, as indicated by irregular fringes.

Fig.2a is a typical HRTEM image of the centrifuged sample. Note the nanoscale grainy texture, showing crystalline particles consisting of some 10-50 lattice spacings (2 - 10 nm). Two dimensional images are clearly seen in many small particles when the [110] zone of the diamond particles is parallel to the electron beam. The exposed surfaces appear to be relatively clean, at most there appears to be a monolayer or two of amorphous structure. The latter is more obvious if the underlying crystallite is not aligned along a low index direction, so that the image is not dominated by high contrast lattice fringes. It seems likely that this amorphous structure occurs as an intergranular phase as well as on exposed (external) surfaces (see discussion § 5(a) below). The corresponding ED pattern is inset in Fig.2a; it shows a diffuse ring pattern typical of essentially randomly oriented polycrystalline grains, with ring diameters consistent with those expected for diamond. The diffraction rings are quite sharp, consistent with the observed particle sizes of 10 - 50 lattice spacings. Individual grains typically show stacking faults and twin interfaces, shown enlarged in Fig.2b for one of the largest grains. Note the clean surface to the left with no indication of graphitic layers.

Fig.3 shows a typical HRTEM image for the uncentrifuged sample; the nanoscale texture is essentially the same as for the centrifuged sample (Fig.2a); however, the exposed surface typically shows two or three fringes typical of graphitic sheet structures,

there is also some amorphous structure evident; again this becomes more obvious for areas of misoriented diamond grains, indicating this is essentially intergranular material. The corresponding EDP (inset in Fig.3) shows the same ring pattern as was obtained for the centrifuged specimen. Weak reflections at 2.46 and 1.41 $\AA$ were indexed as due to 6H hexagonal diamond. The nanoscale diamond crystallites again contained many stacking faults and multiple twins including quintuplets. Dark-field images were also obtained, which allowed the overall distribution of grain diameters to be measured. The size of the diamond particles, measured directly from both the HRTEM and dark-field images, ranged from 2 - 10 nm.

(b) PEELS

Fig.4 shows examples of PEELS results and analyses for CVD and NDP obtained using the JEOL 4000EX instrument; note that for NDP the beam probe included a polycrystalline region some 400 nm in diameter, so that we are averaging over the range of crystal diameters and orientations. The low energy loss-functions are also shown; the spectrum for CVD is typical of diamond, with a characteristic peak at 34 eV and a pronounced shoulder at approx. 23 eV. Note the absence of a significant peak at 5-6 eV, which is characteristic of π^* - plasmons in sp^2 bonded carbons. The NDP spectrum, for an uncentrifuged sample, shows a peak at approx. 20 eV, which is of comparable intensity with a 34 eV peak, there is also a hint of a shoulder at approx. 15 eV. The corresponding core-loss spectra are shown as Fig.4b; again the CVD spectrum is typical of crystalline diamond, with no indication of leading edge fine structure typical of graphite or other varieties of sp^2 bonded carbon. The corresponding NDP spectrum, apart from containing more noise, is again characteristic of sp^3 bonded carbon, again there is no evidence of the existence of any fine structure due to a 1s to π^* peak which would positively indicate the presence of sp^2 bonding states if they existed.

The local mass densities were deduced after measuring the 30 - 34 eV plasmon peak positions in the low loss spectra and applying standard procedures; the results were 3.3 g/cm^3 for uncentrifuges NDP and 3.51g/cm^3 for CVD. The lower value for NDP is consistent with the HRTEM observations of an amorphous integranular phase for the NDPs; this would appear to be essentially amorphous diamond since the core-loss spectra show essentially pure sp^3 bonding. There may also be a contribution to the lowered density from the one ot two graphitic surface layers found on exposed surfaces of NDP aggregates (see Fig.3).

Fig.5 shows a low magnification view of the nanocrystals selected for analysis as well as some PEELS results and analyses from the Phillips CM-20. Crystals labelled A, B and C were selected because they protrude at the edge of the field of view and the 2 nm beam probe could be conveniently located at the center of each without problems of overlapping crystals. Crystals A, B and C have diameters of 7.7, 4.8 and 2.8 nm

respectively.

Fig.5 compares the corresponding low energy loss-functions and core-loss spectra for A, B and C. The loss-function results for crystal A are quite typical of a thin crystal of diamond (c.f. Fig.4 above for CVD diamond), as is the case for the core-loss spectrum. Note that this is the case for crystal A of diameter 7.7 nm, implying that any size effects occur for diameters less than about 10 nm. The corresponding results for crystals B and C are shown in Figs.5. The loss-function for the 4.8 nm nanocrystal B is virtually identical to the NDP result above (c.f. Fig.4), with two maxima at approx. 22 eV and 34 eV and a hint of a shoulder at 15 eV. However, for the 2.8 nm crystal C, the 20 eV peak is stronger than the second peak at approx. 31 eV; note that the overall intensity is also decreased with respect to the zero-loss peak, as one would expect as the crystal thickness decreases. The core-loss spectra essentially retain their sharp leading edges, although for the smallest crystal C there is a small step, probably due to graphitic surface layers as seen Fig.3, which must make a relatively larger contribution as the particle size decreases. There is some noise and loss of detail in the extended fine structure of all the core-loss spectra (Fig.5); this is due to the relatively small number of counts obtained from small volumes with the 2 nm probe, compared with the relatively sharp spectrum obtained for CVD diamond using a 400 nm probe (Fig.4).

5. Discussion

(a) Structure and bonding states of NDP

Our structural results above may be summarized as follows: the NDP formed a polycrystalline aggregate containing crystalline diamond particles 2 - 10 nm diameter. These grains appear to be more or less sintered together with an amorphous or grossly disordered diamond intergranular phase. The carbon bonding is virtually 100 % sp^3. Exposed surfaces of the uncentrifuged sample showed two or three graphitic layers; these are not expected to contribute significantly to the overall properties of the NDP aggregate and appeared to be effectively removed by centrifuging. Thus, conversion to NDP appears to be virtually 100% effective for this fraction of the source powder. Individual crystallites were often highly defective, containing stacking faults, twin boundaries and polytypic diamond intergrowths, including 6H, on {111} planes. Given the small particle size, the presence of essentially amorphous diamond as an intergranular phase is not surprising; thus, considerable disorder should arise quite naturally on contact of the nanoparticles, which may develop into an intergranular phase some 0.3 - 0.5 nm thick following relaxation of the surface atoms in order to mimimize the surface energy by removing dangling bonds, etc. There was no evidence for a preferred orientation of the nanoparticles; thus, there is no evidence for a martensitic transformation from the starting materials to diamond, at least in this case.

(b) Volume plasmons.

Some results from the theory of inelastic scattering of electrons are now introduced; mostly we follow the texbook of Egerton (1986; 1996). Most of the inelastic collisions of a fast electron arise from interaction with electrons in outer atomic shells and result in an energy loss of less than 100 eV. In a solid, the major contribution comes from valence electrons (referred to as conduction electrons in a metal). In response to an external electric field, such as that produced by an incident electron, a collective oscillation of the electron density occurs at a characteristic angular frequency ω_p; it is necessary to introduce an effective mass m for the electrons, which differs from their rest mass m_o, as well as a damping constant Γ and a relaxation time τ. The behaviour of the free electron gas is described in terms of the relative permittivity or dielectric function

$$\epsilon(\omega) = \epsilon_1 + i\epsilon_2 = 1 - \omega_p^2/(\omega^2 + \Gamma^2) + i\Gamma\omega_p^2/[\omega(\omega^2 + \Gamma^2)] \quad (1)$$

Here ω is the angular frequency (rad.s^{-1}) of forced oscillation and ω_p is the resonance frequency for plasma oscillation, defined by

$$\omega_p = [ne^2/(\epsilon_o m)]^{\frac{1}{2}} \quad (2)$$

The energy-loss function is defined as

$$Im[-1/\epsilon(E)] = \epsilon^2/(\epsilon_1^2 + \epsilon_2^2) = \omega\Gamma\omega_p^2/(\omega^2 - \omega_p^2)^2 \quad (3)$$

An incident electron represents a sudden impulse of applied electric field, containing all angular frequencies (Fourier components). Setting up a plasma oscillation of the outer-shell electrons at an angular frequency ω_p is equivalent to creating a "pseudoparticle" of energy $E_p = \hbar\omega_p$, called the plasmon (Pines, 1963). As shown by Egerton (1986), the energy dependence of the single-scattering inelastically scattered intensity (the energy-loss spectrum) is proportional to Im[-1/$\epsilon(E)$] (the loss-function), in which the variable $E = \hbar\omega$ represents energy loss.

(c) Single-electron excitations.

Above a certain wave vector $q_c = E_p/\hbar v_F$, where v_F is the Fermi velocity, the plasmon oscillations in a "free electron gas" are heavily damped because it becomes possible for a plasmon to transfer all of its energy to a single electron, which can then undergo an interband transition. The observable effects of single-electron excitation include the addition of fine structure to the energy-loss spectrum and a broadening (and possibly a shift) of the plasmon peak. In an insulator or semiconductor, practically all of the electrons have a binding energy at least equal to the band gap E_g); this produces (Raether, 1980) a new plasmon energy

$$(E_p^i)^2 \cong E_p^2 + E_g^2 \tag{4}$$

For diamond the predicted value of E_p (after applying Eq.(2)) is 31 eV and the upwards shift of the plasmon energy is predicted to be only about 0.6 eV. In fact, the observed plasmon energy for crystalline diamond is typically 34 eV, compared to the predicted value of 31.6 eV; these values are thus not totally explained by this theory.

(d) Surface plasmons.

There also exist longitudinal waves of charge density which travel along a surface; these are known as surface plasmons. The electrostatic potential at the surface, assumed here to be planar, is of the form $cos(qx - \omega t)exp(-q \mid z \mid)$, where q and ω are the wave vector and angular frequency of oscillation and t represents time. The charge density at the surface is proportional to $cos(qx - \omega t)\delta(z)$ and electrostatic boundary conditions lead to a condition (Egerton, 1986)

$$\epsilon_a(\omega) + \epsilon_b(\omega) = 0 \tag{5}$$

where ϵ_a and ϵ_b are the relative permittivities on either side of the boundary. This equation defines the angular frequency ω_s of the surface plasmon.

The simplest situation corresponds to a single vacuum/metal interface where the metal has negligible damping ($\Gamma = 0$). Then: $\epsilon_a = 1$ and $\epsilon_b = 1$ - ω_p^2/ω^2, where $\omega_p = E_p/\hbar$ is the bulk plasmon frequency in the metal. Substitution into Eq.(5) gives the energy E_s of the surface plasmon peak in the energy-loss spectrum

$$E_s = \hbar\omega_s = \hbar\omega_p/\sqrt{2} = E_p/\sqrt{2} \tag{6}$$

The width of the plasmon peak is determined by the imaginary parts of the permittivities on both sides of the boundary. The surface plasmons excited on each surface of a specimen of thickness t are essentially independent of each other provided that

$$q_s t \cong k_o \theta t \gg 1 \tag{7}$$

where $k_o = 1700$ nm^{-1} is the incident wave vector For 100 keV electrons and the scattering angle $\theta \simeq \theta_E/\sqrt{3} \simeq 0.1$ mrad. Eq.(7) implies $t \gg 10$ nm. If this condition is not fulfilled, the electrostatic fields originating from the two surfaces overlap and the plasmons can interact with one another (see Fig.3.22 of Egerton, 1986). In the case of a free-electron metal bounded by similar dielectrics ($\epsilon_a = \epsilon_c = \epsilon$; $\epsilon_b = 1 - \omega_p^2/\omega^2$) the resonance is split into two modes, the frequency of each being q-dependent and given approximately, for large q_s, by (Ritchie, 1957)

$$\omega_s = \omega_p[\frac{1 \pm exp(-q_s t)}{1 + \epsilon}]^{\frac{1}{2}} \tag{8}$$

The symmetric mode, where like charges are opposite one another, corresponds to the higher angular frequency. Further equations for the scattering probabilities for surface plasmons, including reference to relativistic correction, etc are discussed further by Egerton (1986) and Raether (1980).

Of direct interest for the discussion to follow we now summarize some results for surface modes in small spherical particles (see e.g. Egerton, 1986 or Raether, 1980). In the case of an isolated spherical particle (relative permittivity = ϵ_b) surrounded by a medium of permittivity ϵ_a, the surface resonance condition is modified from Eq.(5) to become

$$\epsilon_a(l+1)/l + \epsilon_b = 0 \tag{9}$$

where l is an integer. For a free-electron metal, Eq.(9) gives, for the surface-resonance frequency

$$\omega_s = \omega_p[1 + \epsilon_a(l+1)/l]^{-\frac{1}{2}} \tag{10}$$

where ϵ_a is the relative permittivity of the immediate surroundings (e.g. vacuum or a surface or oxide layer). The lowest frequency corresponds to $l = 1$ (the dipole mode) and predominates in very small spheres, of radius $r \ll 10$ nm. Several independent theoretical approaches agree that the surface plasmon mode energies do not shift significantly with radius, although the probability of excitation over the different modes does favour higher orders for increasing size; thus, as the radius increases, the resultant energy-loss intensity shifts to higher-order modes and the resonance-frequency increases asymptotically towards the value of Eq.(6) for a flat surface.

Some examples of surface plasmon frequencies expected for spherical diamond particles are shown in Table 1; these were calculated using Eq.(10) and assuming $E_p = 34$ eV. These predictions will be referred to in section (e) below.

The subject of appropriate quantum solutions for surface plasmons, including possible confinement effects is developing in the literature. Ouyang, Batson and Issacson (1992) investigated quantum size effects in the surface-plasmon excitation of small silver particles (4 - 20 nm) by EELS; Wang and Cowley (1987) showed that it may be necessary to account for surface-oxide/particle and particle/substrate interfaces as well as the small particle resonances in the case of aluminum spheres on AlF_3 substrates; more recently Aizpurna, Rivacoba and Apell (1996) claimed to have explained some anomalous results due to Ouyang et al (1992), Wang and Cowley (1987) and others using a macroscopic dielectric formalism.

We should also mention the experimental results of Bursill, Stadelmann, Peng and Prawer (1994), who observed 15 eV surface plasmons for nanotubes containing fewer than 5 - 7 graphitic sheets, and the theoretical work of Yannouleas, Bogachek and Landman (1996) on plasmons in carbon nanotubes.

(e) Interpretation of loss-function results.

The loss-function of CVD (Fig.4) showed a dominant peak at 34ev with half width of about 14ev; this is characteristic of crystalline diamond (see e.g. Daniels et al (1970), Egerton and Whelan (1974); it is interpreted as due to the collective excitation of valence electrons (volume plasmon) plus a contribution from single electron excitations according to Eq.(4) above. The half width of 14 eV corresponds to a relatively large damping constant Γ so that the plasmon oscillation is effectively damped after only 0.14 of an oscillation. There is also a shoulder at 23ev; this has been tentatively interpreted as a surface plasmon, excited as the incident electron crosses the top or bottom surfaces of thin ($\ll$ 50 nm) specimens, with angular frequency according to Eq.(6) above (see discussion by Egerton and Whelan, 1974). However, it has also been interpreted as an interband transition (Daniels et al, 1970; Fink, 1989); these authors remark "this transition is not yet identified in the band scheme but the transmission loss experiments confirm that it is intrinsic to diamond". We note that comparison of the loss function for diamond with optical data, as was made originally by Daniels et al, does seem to be consistent with their conclusion that the shoulder at 23 eV is an intrinsic bulk dielectric property of diamond. In principle there must be surface plasmons; however, they will not be apparent in the loss function until the crystal becomes thin enough for surface plasmon intensity to become significant.

For NDP crystal A (diameter 7.7 nm) the loss-function has this same distinctive shape, with a shoulder at 23 eV and a peak at about 34 eV (cf. Figs.4,5). As the particle size decreases the 34 eV peak shifts down 0.8-1.2 eV to 32.8-33.8 eV and its FWHM increases to about 28 eV, which is much broader than for CVD. At the same time the intensity of the 22.8 eV peak shifts down to approx. 19.5 eV and increases in intensity, so that the loss-function appears as two overlapping peaks (see Fig.5); finally the lower energy peak dominates (see Fig.5). Given the discussion in section (d) above it seems reasonable to interpret the behaviour of the lower energy peak as representing plasmon oscillations associated with the 2 - 8 nm (roughly spherical) diamond nanocrystals observed above by HRTEM. It appears that the changeover from effectively bulk behaviour begins for diameters below approx. 10 nm and may almost complete at approx. 2 nm. For the smallest particles, where the $l = 1$ dipole mode should dominate the intensity, we expect surface plasmon energy of 19.4 eV. As the particle size increases, higher order modes should increasingly contribute until the surface is essentially flat, when $\hbar\omega_s = 24.0$ eV. These predictions are in excellent agreement with the results shown in Fig.5 and Table 1 above for $l = 1$, 3 and ∞. Note that we have made the reasonable assumption that the particles may be modelled as more or less spherical and we have ignored the possible effects of any amorphous intergranular phase. The latter is not expected to contribute greatly since the refractive index may not differ appreciably from crystalline diamond.

Note that we have no evidence which necessarily contradicts the interpretation of the 23 eV shoulder for thicker crystals of diamond (say $\gg$ 100 nm) as an interband transition, intrinsic to "bulk diamond". However, it is very clear that the size effects just discussed are simply explained in terms of the predicted properties of surface plasmon oscillations of spherical diamond particles. Comparing the results for NDP with our results for CVD diamond it is also clear that the contribution from the 23 eV surface plasmon peak does diminish significantly with increasing thickness (c.f. also the results published by Egerton and Whelan (1974) for thicknesses of 200 nm and 100 nm), as one expects for surface plasmons.

It is also worth noting that the electronic properties of NDP may themselves be modified as the particle size decreases; thus the two effects, surface plasmon versus interband transition, may become decoupled as the size decreases, when the surface plasmon dominates. There was no significant observable variation of the core-loss fine structure as the particle size decreased.

6. Conclusion

Combined HRTEM, SAD and PEELS analysis has allowed us to evaluate the bonding state, the local density and nanostructure of NDP diamond. The presence of amorphous diamond and the absence of all but a small trace of graphite was shown clearly. The morphology, crystal structure and defects structures of the NDP were also obtained.

We have clearly demonstrated that there are very significant size effects on the plasmon component of the dielectric response of NDP, which onset for particle size below approx. 10 nm and become increasingly significant down to 2.8 nm.

We expect that, with further refinement of the PEELS analysis, the set of techniques applied above for diamond will also prove valuable for other wide gap materials with interesting dielectric properties, especially when these are subject to deliberate modification on the nanoscale.

Acknowledgements

This work was supported financially by the Australian Research Council. We are grateful for support of the HRTEM and PEELS facilities at the University of Melbourne by David Dryden and NAMAC and also for access to the Phillips CM20 instrument at Department of Materials Engineering at Monash University. The NDP specimen was obtained from Dr. Peter Belobrov of the Institute of Biophysics, Krasnoyarsk and the CVD diamond was provided by Dr. Patrice Gonon.

REFERENCES

Aizpurna, J., Rivacoba, A., and Apell, S.P., Phys. Rev. B54 (1996) 2901-2909.

Bursill, L.A., Stadelmann, P.A., Peng, J.L., and Prawer, S., Phys.Rev. B49 (1994) 2882-2887.

Daniels, J., Festenberg, C.V., Raether, H., and Zeppenfeld, K., "Optical Constants of Solids by Electron Spectroscopy", Springer Tracts in Modern Physics, Springer-Verlag, New York, Vol. 54, pp 78 - 135 (1970).

Egerton, R.F. and Whelan, M.J., Phil. Mag., 30 (1974) 739-749.

Egerton, R.F. *Electron Energy Loss Spectroscopy in the Electron Microscope* , First Ed. New York, (1986); ibid Second Ed. (1996).

Erskine, D.J. and Nellis, W.J., Mat. Res. Soc. Symp. Proc. Vol 270, 437-442 (1992).

Fink, J., Adv. in Electronics and Electron Physics, 75 (1989) 121-232.

Ouyang, F., Batson, P.E., and Issacson, M., Phys. Rev., B46 (1992) 15421-15425.

Peng, J.L., Fan, X.D. and Bursill, L.A., Inter. J. Mod. Phys.B, in press (1996).

Pines, D., "Elementary Excitations in Solids", Benjamin, New York (1964).

Prawer, S., Nugent, K.W. et al, "Micro-Raman study of diamond powders", in preparation (1996).

Raether, H., "Excitation of Plasmons and Interband Transitions by Electrons", Springer-Verlag, Berlin (1980)

Ritchie, R.H., Phys. Rev., 106 (1957) 874-881.

Wang, Z.L., and Cowley, J.M., Ultramicros., 21 (1987) 77-94; ibid 21 (1987) 335-346; ibid 21 (1987) 347-366; ibid 23 (1987) 97-108.

Yannouleas, C., Bogachek, E.N., and Landman, U., Phys. Rev. B53 (1996) 10225-10236.

Figure Captions

Figure 1
HRTEM images of CVD diamond for $[01\bar{1}]$ direction; note stacking faults on (111) and $(\bar{1}11)$ lattice planes and the 1 nm surface layer.

Figure 2
(a) HRTEM image of centrifuged sample, showing NDP sizes of 20 - 80 Å. The external surfaces are clean with, at most, a non-crystallin monolayer or two. An ED pattern (inset) shows reflection rings characteristic of diamond.
(b) Enlargement from (a) showing intergrowth defects on (111).

Figure 3
HRTEM images of uncentrifuged NDP: ED pattern is inset; some particles show amorphous surface layers and external surfaces show two or three layers typical of graphitic sheets.

Figure 4
PEELS results for CVD diamond and NDP obtained using a 400 nm probe. The low energy loss-functions both show a broad peak at 34 eV, CVD diamond has a shoulder at 24 eV whereas NDP has a peak at 20 eV. The corresponding core-loss spectrum for CVD shows a leading edge typical of pure sp^3 bonding for CVD whereas there is a hint of a small sp^2 contribution for NDP.

Figure 5
Showing the nanocrystals A (7.7 nm), B (4.8 nm) and C (2.8 nm) of NDP selected for PEELS analysis using a 2 nm elecron probe. The loss-functions for crystal A is similar to that for CVD diamond (c.f. Fig.4 above), B is almost identical with the result averaged over the 400 nm probe (c.f. Fig.4 above) whereas for C the first peak is at 19.5 eV and is larger than the 32 eV peak. The core-loss spectra for crystals A, B and C show some degradation of the fine structure for decreasing size and a small SP^2 contribution.

Table.1 Observed and predicted plasmon energies for nanocrystalline diamond powder

Mode order l	Predicted E_s eV	Measured E_s eV	Particle Size nm	Measured E_p eV
1	19.62	19.5	2.8	30.0
2	21.50	-	-	-
3	22.25	22.5	4.8	32.0
∞	24.04	24.0	7.7	34.0

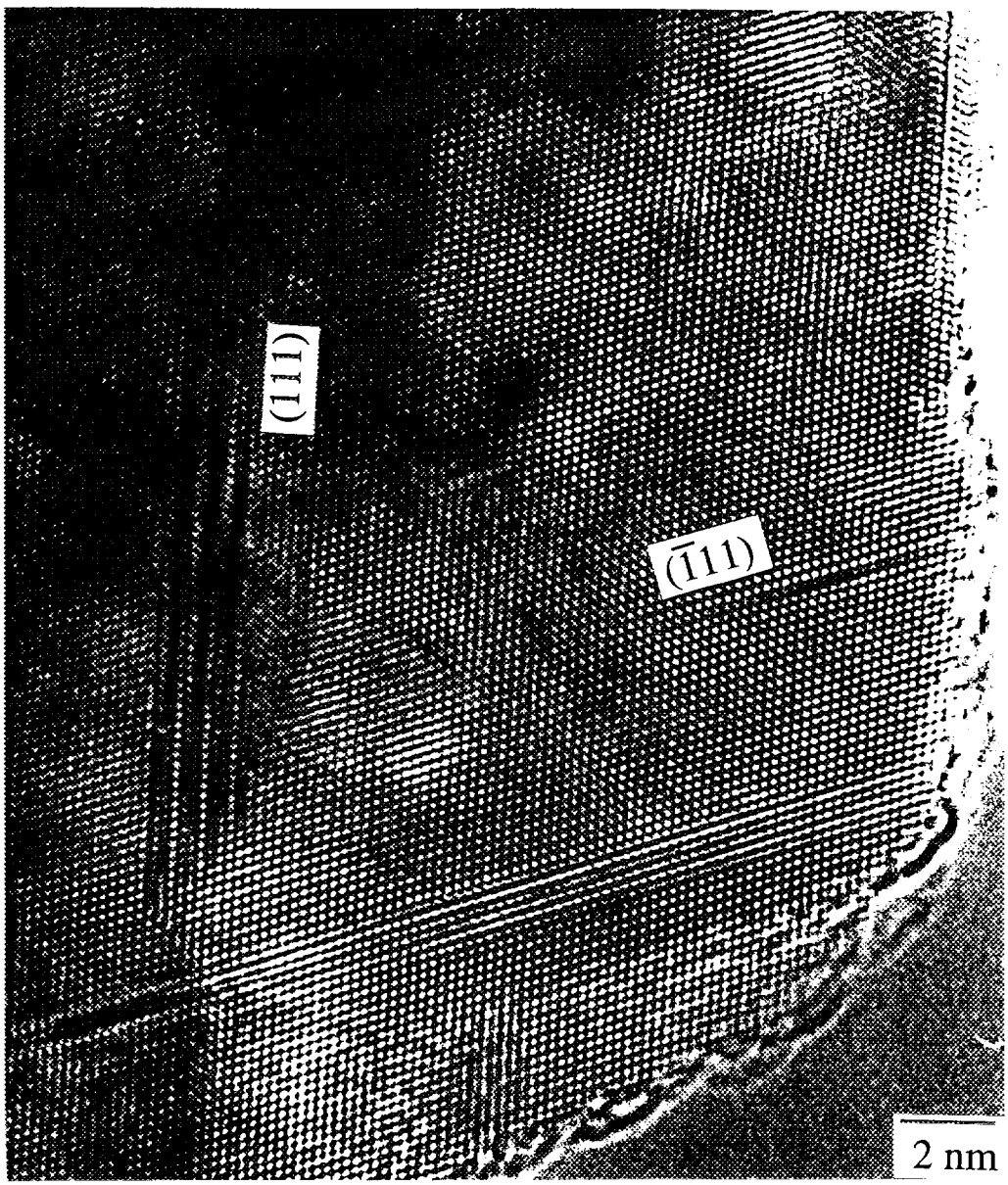

FIGURE 1

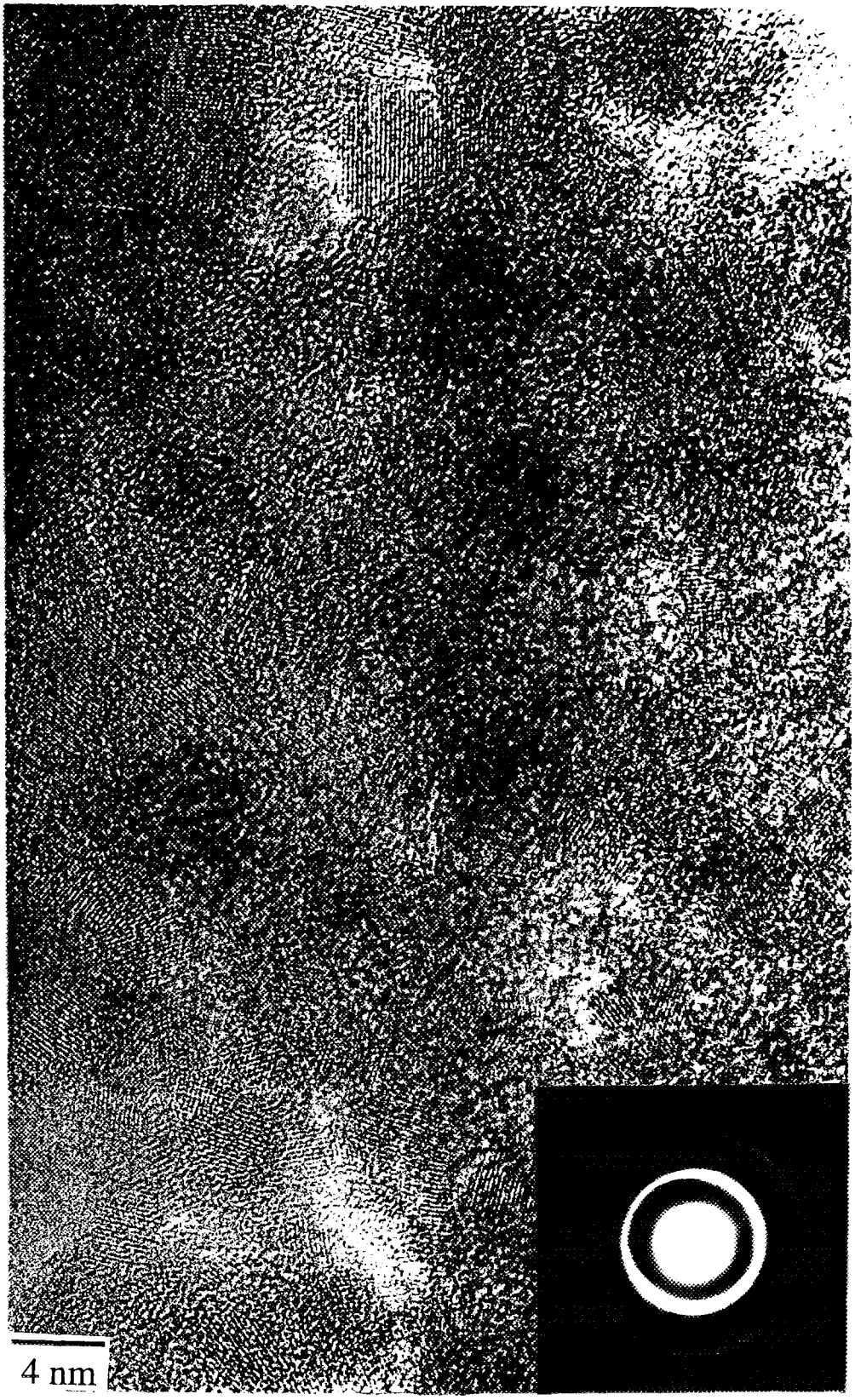

FIGURE 2(a)

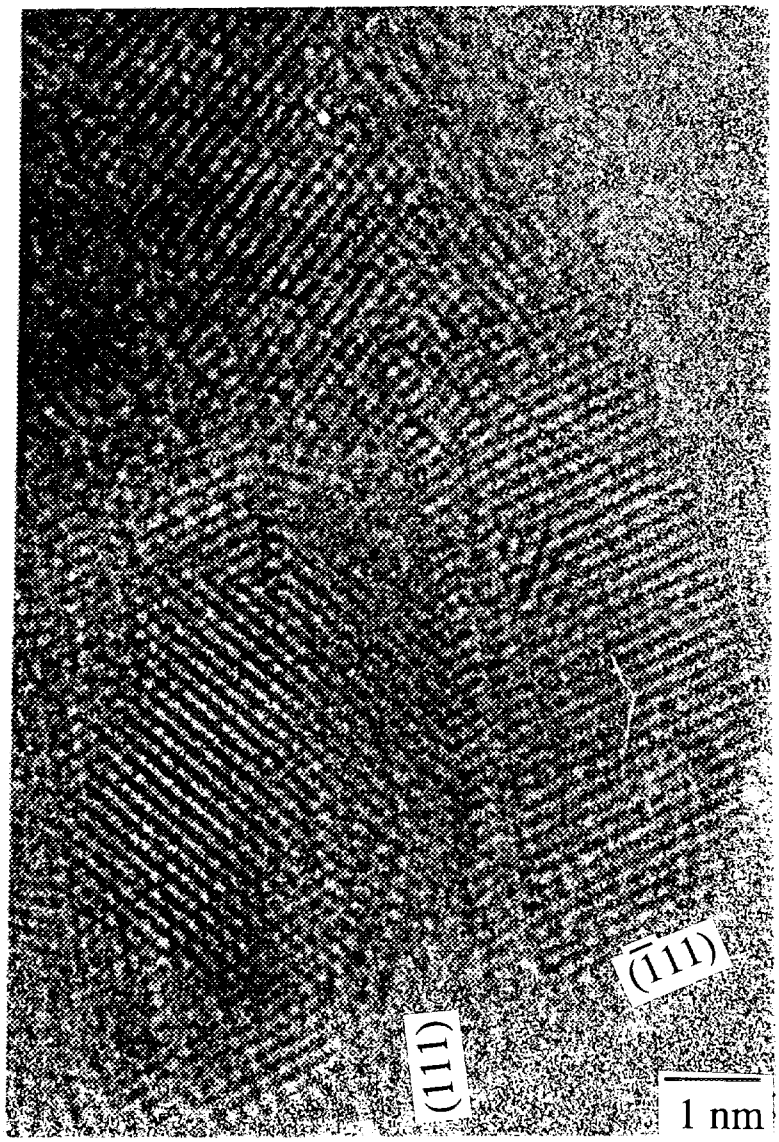

FIGURE 2(b)

FIGURE 3

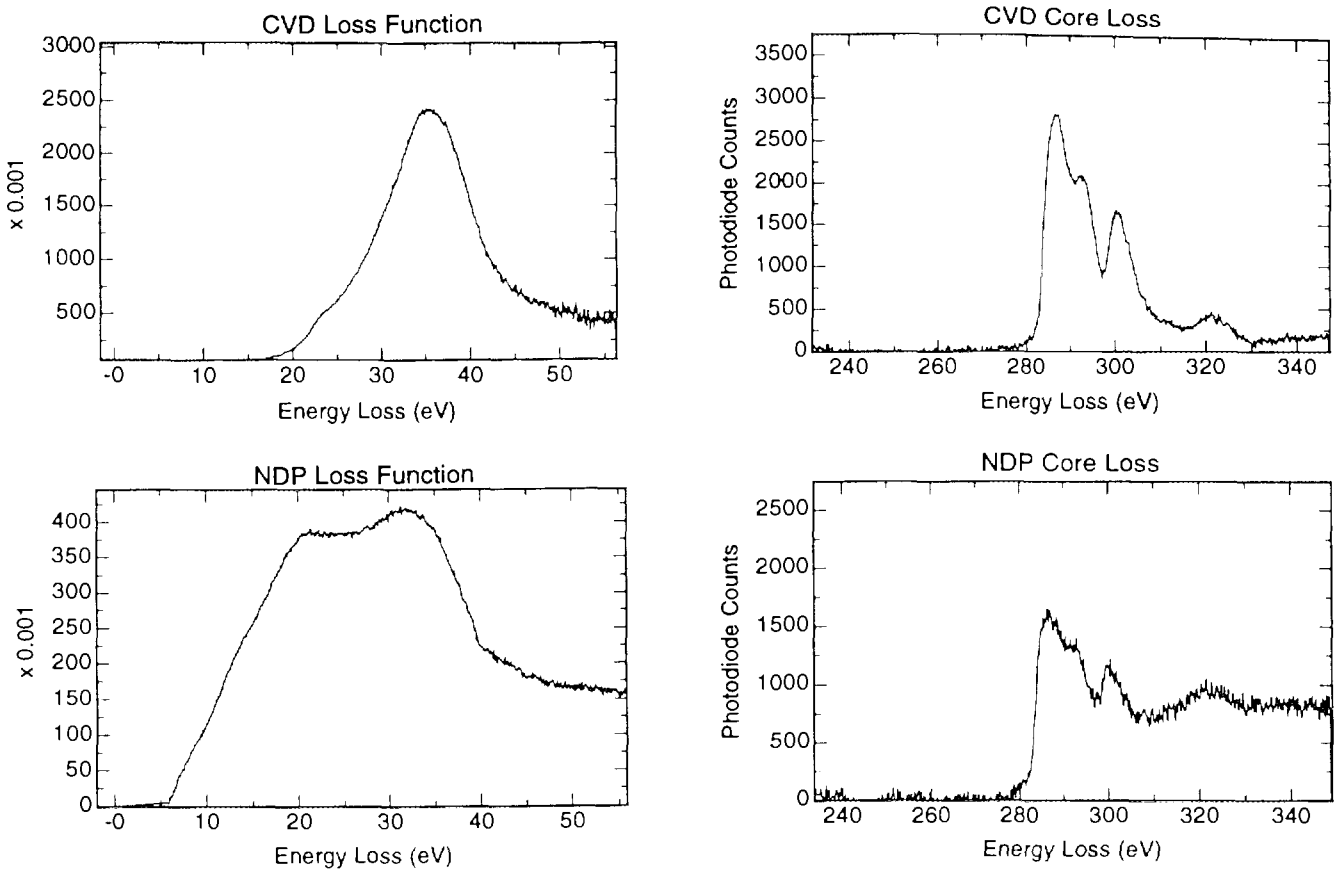
CVD Loss Function
x 0.001
3000
2500
2000
1500
1000
500
-0
10
20
30
40
50
Energy Loss (eV)
CVD Core Loss
Photodiode Counts
3500
3000
2500
2000
1500
1000
500
0
240
260
280
300
320
340
Energy Loss (eV)
NDP Loss Function
x 0.001
400
350
300
250
200
150
100
50
0
-0
10
20
30
40
50
Energy Loss (eV)
NDP Core Loss
Photodiode Counts
2500
2000
1500
1000
500
0
240
260
280
300
320
340
Energy Loss (eV)

FIGURE 4

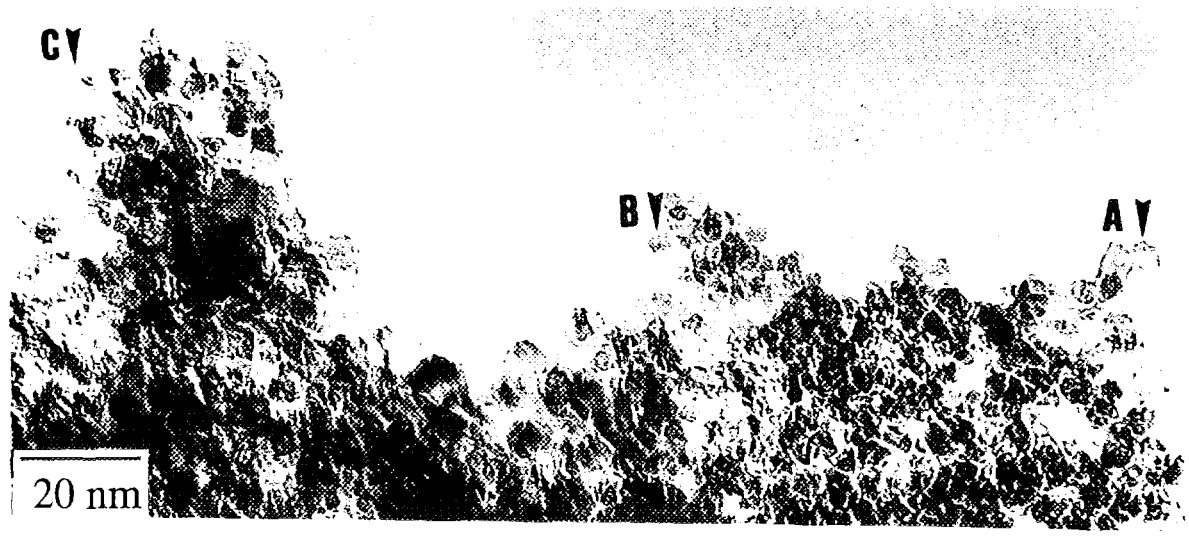
C
B
A
20 nm

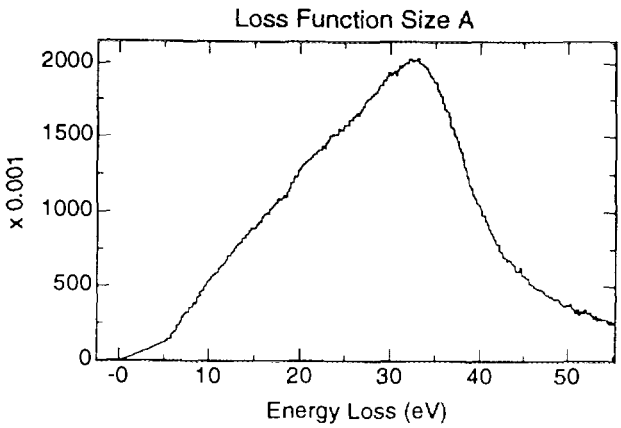
Loss Function Size A
x 0.001
2000
1500
1000
500
0
-0
10
20
30
40
50
Energy Loss (eV)

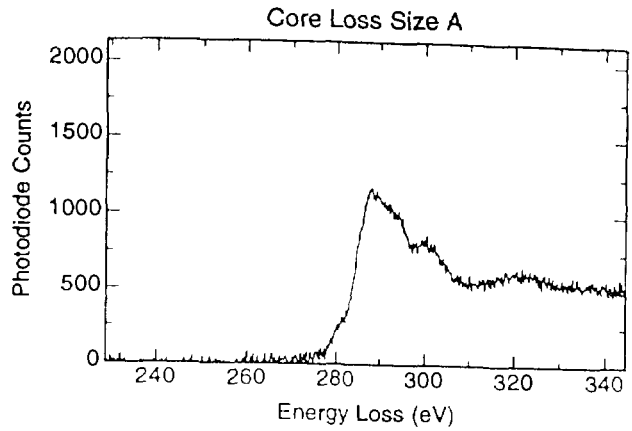
Core Loss Size A
Photodiode Counts
2000
1500
1000
500
0
240
260
280
300
320
340
Energy Loss (eV)

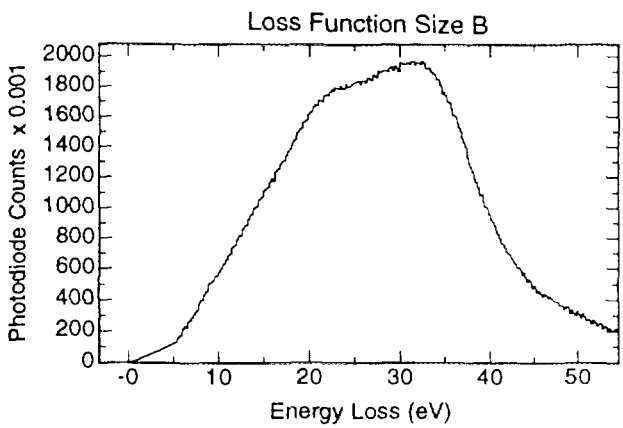
Loss Function Size B
Photodiode Counts x 0.001
2000
1800
1600
1400
1200
1000
800
600
400
200
0
-0
10
20
30
40
50
Energy Loss (eV)

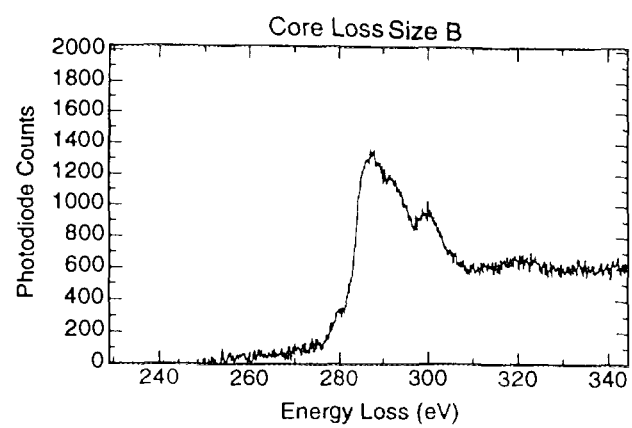
Core Loss Size B
Photodiode Counts
2000
1800
1600
1400
1200
1000
800
600
400
200
0
240
260
280
300
320
340
Energy Loss (eV)

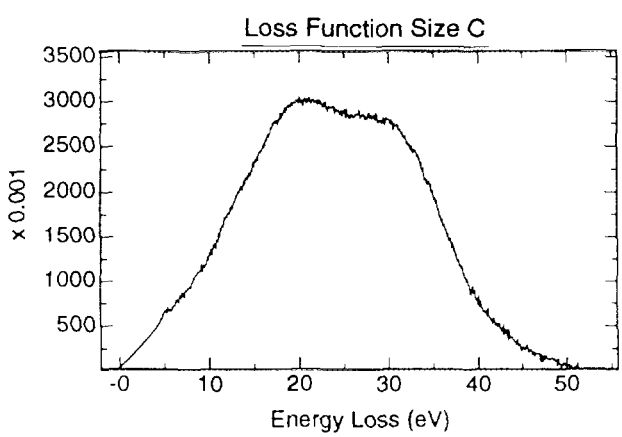
Loss Function Size C
x 0.001
3500
3000
2500
2000
1500
1000
500
-0
10
20
30
40
50
Energy Loss (eV)

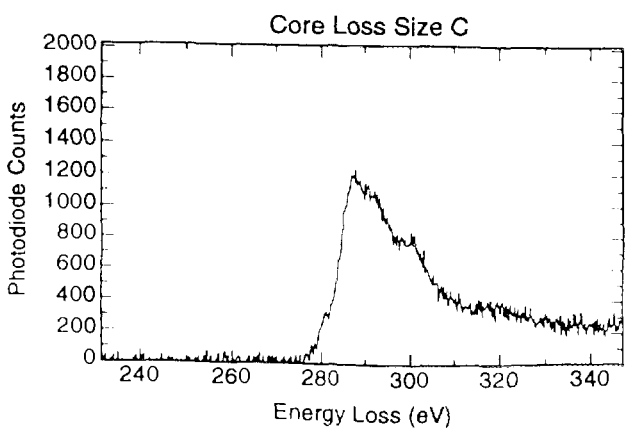
Core Loss Size C
Photodiode Counts
2000
1800
1600
1400
1200
1000
800
600
400
200
0
240
260
280
300
320
340
Energy Loss (eV)

FIGURE 5